International Journal of Plasticity 162 (2023) 103524

Contents lists available at ScienceDirect

International Journal of Plasticity

journal homepage: www.elsevier.com/locate/ijplas

CRSS determination combining ab-initio framework and Surrogate Neural Networks

Daegun You[a,#], Orcun Koray Celebi[a,#], Ahmed Sameer Khan Mohammed[a], Diab W. Abueidda[a,b], Seid Koric[a,b], Huseyin Sehitoglu[a,*]

[a] *Department of Mechanical Science and Engineering, University of Illinois at Urbana-Champaign, 1206 W. Green St., Urbana, IL 61801, United States*

[b] *National Center for Supercomputing Applications, University of Illinois at Urbana-Champaign, 1205W. Clark St., IL 61801, United States*

A R T I C L E I N F O

Keywords:
Critical stress
Dislocations
Machine learning
Surrogate Neural Network
Wigner-Seitz cell

A B S T R A C T

Critical Resolved Shear Stress (CRSS), fundamentally linked to the dislocation glide stress, is a crucial measure in dictating plastic deformation in metallic materials. A recent ab-initio predictive model for dislocation glide stress in Face-Centered Cubic (FCC) materials is developed which accurately predicts available experimental data, considering the anisotropic continuum energy, the atomistic misfit energy, and the minimum energy path for the intermittent motion of Shockley partials. The CRSS of a material is predominantly controlled by six parameters, namely, lattice constant, unstable/stable stacking-fault energies, and three anisotropic elastic constants for cubic materials, which are inputs to the predictive model. In this work, a large material dataset is produced incorporating properties of real materials and generating hypothetical combinations, subsequently calculating the CRSS for each combination using the predictive model. The hypothetical combinations of properties are employed to train a machine learning-based Surrogate Neural Network (SNN), and the ones of real materials are utilized to validate the SNN model yielding a 94% accuracy for 1,033 materials. The generated dataset is used to unravel the sensitivity of each material parameter to the predicted CRSS establishing a general trend for the FCC materials for the first time guiding the field in achieving superior mechanical properties.

1. Introduction

Critical Resolved Shear Stress (CRSS) determines yield strength which is one of the most important mechanical properties of a material (Argon, 2007). The continuous deformation of the material at its yield point transforms it into its inelastic status, and this threshold is dictated by the CRSS defined as the stress required for the onset of dislocation glide. In the compositional complexity of materials, however, a comprehensive understanding of the CRSS has been yet unclear with respect to core-width and effect of dislocation characters. Original treatments of the CRSS calculation utilized simple-cubic lattices (Nabarro, 1947; Peierls, 1940), and performed integration for misfit energy based on the one-dimensional description, which is a limitation of Peierls-Nabarro model (Schoeck, 2005). Meanwhile, an ab-initio framework for the CRSS suggested by Mohammed-Celebi-Sehitoglu (MCS) (Mohammed et al., 2022), which is free of empirical parameters, has been recently proposed as a predictive alternative. It has uncovered that CRSS

---

[*] Corresponding author.
E-mail address: huseyin@illinois.edu (H. Sehitoglu).
[#] Both authors contributed equally to this paper

https://doi.org/10.1016/j.ijplas.2023.103524
Received 6 October 2022; Received in revised form 9 December 2022;
Available online 13 January 2023

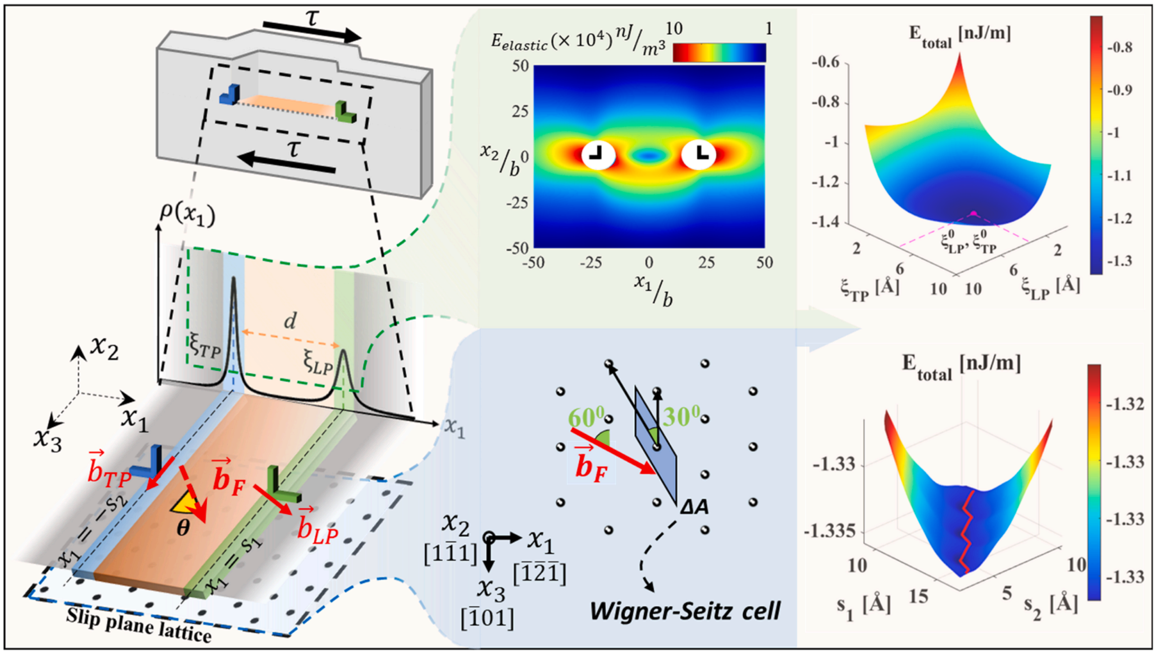

Fig. 1. Schematic of the ab-initio CRSS framework introduced by Mohammed-Celebi-Sehitoglu (MCS); For a given core structure of an extended dislocation in FCC materials, $\vec{b}_F = a/2[\overline{110}]$ is the Burgers vector of full dislocation on a $(1\bar{1}1)$ plane, $\vec{b}_{TP} = a/6[\overline{121}]$ a leading partial, $\vec{b}_{TP} = a\ /\ 6[\overline{211}]$ a trailing partial, and d a stacking fault bounded by the two partials, where a given lattice constant a; The current study sets 60° mixed character of dislocation as an instance in the given coordinate system; In the plot of the dislocation-density distribution $\rho(x_1)$, the leading partial is at position $x_1 = s_1$, and the trailing partial is at $x_1 = -s_2$, yielding the fault-width as $d = s_1 + s_2$, while the core-widths are ξ_{TP}, ξ_{LP} of the trailing and leading partials respectively; Total energy (alluded to in the main text) of extended dislocation includes strain and misfit energies, which are based on anisotropy interaction elastic energy and Wigner-Seitz (WS) cell definition, respectively.

results are consistent with previous experiments, including pure metals as well as high entropy alloys (HEAs). Upon sophisticated consideration of the anisotropic continuum elastic energy and atomistic misfit energy employing the Wigner-Seitz cell Misfit (WS-M) model the predictive framework calculates the CRSS of the extended dislocation through an energy minimization approach. The anisotropic strain energy is obtained by employing the Eshelby-Stroh (E-S) framework that captures the coupled interaction between the edge and screw components of the dislocation and yields an accurate estimate of the continuum energy. The core energy of the dislocation is precisely captured with the WS-M model which incorporates exact atomic sites by being faithful to the two-dimensional structure of the slip-plane. The equilibrium structure of the extended dislocation is obtained through an energy-minimization method involving both energy components. The minimum energy path (MEP) for the glide of the extended dislocation is determined, suggesting an intermittent motion of Shockley partials. The associated CRSS to the energy trajectory is obtained from the novel Optimum-Energy-Trajectory (OET) approach which considers gradients of motion of the individual partials. Thus, the robustness of the predictive framework makes it useful for the exploration of the large compositional space of Face-Centered Cubic (FCC) materials.

The introduced MCS framework (Mohammed et al., 2022) for the CRSS requires only six fundamental material properties (or fingerprints) as input parameters: lattice constant, unstable/stable stacking-fault energies, and three elastic constants for cubic materials, all of which can be reliably obtained from first-principles calculations. Thus, the predictive model achieves precise prediction of the CRSS, shown to be in excellent agreement with the experimental data, can be utilized to uncover the large compositional space circumventing time-consuming expensive experiments, and provides a tool for rapid assessment of a material strength (Brenne et al., 2020; Gengor et al., 2021; Li et al., 2020; Mohammed and Sehitoglu, 2020; Nöhring and Curtin, 2020; Panchal et al., 2013; Ritchie, 2021; Sidharth et al., 2021). Although the proposed framework is necessary for materials design in a wide compositional space, accurate material properties should be provided as input to the model for a precise prediction. For some complex materials, e.g., multi-principal element alloys, the input parameters are not readily available and require costly experiments or intensive atomistic simulations for accurate determination (Celebi et al., 2022a; Chowdhury et al., 2015; Kibey et al., 2006; Li et al., 2014; Li et al., 2022; Mohammed et al., 2022; Werner et al., 2021). In addition, the determination of the core structure of the extended dislocation and MEP for glide remains a bottleneck since the validity of results should be examined for every single material with a low tolerance on the minimization of total energy. Hence, an alternative methodology that bypasses this time-consuming process enabling immediate prediction of the CRSS should be established.

As for an effective model that can readily predict material properties, machine learning (ML) has recently been utilized in material design and optimization of properties (Abueidda et al., 2022; Abueidda et al., 2021a; Goli et al., 2020; Kollmann et al., 2020; You et al., 2022). Learning from a large dataset via experiments or ab-initio calculations, ML has a time-effective advantage in predicting properties after learning. ML-based neural network models have also been used to surrogate the existing computational theories with the obtained data (Abueidda et al., 2021b; Guo et al., 2020; Shahane et al., 2022). In this work, the Surrogate Neural Networks (SNN) model for the CRSS prediction of mixed dislocation slip in FCC materials is developed using the datasets obtained from the novel ab-initio predictive framework. The workflow of this study is broken into four steps: 1) Parametric study of the CRSS of FCC within individual materials' fingerprints, 2) Producing a large dataset of general FCC materials for the SNN, 3) Training and test of the SNN model, and 4) High dimensional analyses of characteristics that dictate the CRSS. The current study establishes a novel triangular trajectory as the MEP that implies the least resistance for the glide of Shockley partials. The large dataset of general FCC materials is composed of hypothetical materials as training data with arbitrary combinations of the six parameters (lattice constant (a), unstable/intrinsic stacking-fault energies (γ_{us}, γ_{isf}), and three elastic constants (C_{11}, C_{12}, C_{44}) for cubic systems). Then, real materials are used as test data employing their properties given in the literature. Subsequently, we perform a sensitivity analysis for a better understanding of the effect of the individual parameters on the predicted CRSS.

2. Methods and results

2.1. Analytical framework

Fig. 1 represents the schematic of the ab-initio predictive framework to calculate core widths, stacking-fault, and finally, Critical Resolved Shear Stress (CRSS) of the extended dislocation. For current study, we focus on the CRSS of the mixed character of dislocation as the overall material strength, since the framework has recently found the maximum CRSS upon analyzing the entire spectrum of dislocation characters (Celebi et al., 2022b). This CRSS framework suggested by Mohammed-Celebi-Sehitoglu (MCS) (Mohammed et al., 2022) incorporates sophisticated calculations of the anisotropic elastic interaction, the atomistic misfit energy, and the energy-minimization of intermittent motion of Shockley partials. The dislocation density distributions ($\rho(x_1)$) are derived from the core disregistry distributions ($f(x_1)$) of the leading (LP) and trailing partials (TP), respectively. Both the core disregistry distributions $f(x_1)$ and dislocation density distributions $\rho(x_1)$ are defined as the following equations:

$$f_{LP}(x_1) = \frac{b_p}{2} + \frac{b_p}{\pi}\tan^{-1}\left(\frac{x_1 - s_1}{\xi_{LP}}\right);\ \rho_{LP}(x_1) = \frac{b_P}{\pi}\left(\frac{\xi_{LP}}{(x_1 - s_1)^2 + \xi_{LP}^2}\right) \tag{1}$$

$$f_{TP}(x_1) = \frac{b_p}{2} + \frac{b_p}{\pi}\tan^{-1}\left(\frac{x_1 + s_2}{\xi_{TP}}\right);\ \rho_{TP}(x_1) = \frac{b_P}{\pi}\left(\frac{\xi_{TP}}{(x_1 + s_2)^2 + \xi_{TP}^2}\right) \tag{2}$$

where b_p is the magnitude of the Burgers vector of partials, and the positions of LP and TP are at s_1 and $-s_2$, which determines the stacking fault width $d = s_1 + s_2$. Eqns. (1) and (2) show that the core structure of the extended dislocation with several key parameters; the core-width ξ_{LP} and ξ_{TP} of the LP and TP, and the stacking fault width d. The determination of these parameters is then based on the energy-minimization. The MCS framework involves the minimization of the total energy (E_{total}) of the extended dislocation in FCC materials composed of the two energy components. Thus, E_{total} is expressed as,

$$E_{total}(\xi_{LP}, \xi_{TP},\ s_1, s_2) = E_{strain}(\xi_{LP}, \xi_{TP},\ s_1, s_2) + E_{misfit}(\xi_{LP}, \xi_{TP},\ s_1, s_2) \tag{3}$$

where E_{strain} is the elastic strain-energy based on the anisotropic Eshelby-Stroh (E-S) formalism (Barnett and Lothe, 1974; Stroh, 1958), and E_{misfit} is the misfit energy of the extended dislocation computed utilizing the Wigner-Seitz (WS) cell area misfit model that considers the WS cell domain area at each atomic-site on the slip plane across which disregistry prevails. For the details of the elastic strain-energy and misfit energy formalism, the reader may refer to elsewhere (Mohammed et al., 2022).

The total continuum strain energy $E_{strain}(\xi_{LP}, \xi_{TP},\ s_1, s_2)$ for the extended dislocation can be determined by computing the anisotropic interaction coefficients. The total strain energy $E_{strain}(\xi_{LP}, \xi_{TP},\ s_1, s_2)$ consists of the self-interaction energies of the LP and TP (such as $E_{elastic}^{11}$ and $E_{elastic}^{22}$, respectively) and the interaction energy between the two partials ($E_{elastic}^{12}$). Therefore, $E_{strain}(\xi_{LP}, \xi_{TP},\ s_1, s_2)$ is expressed as,

$$E_{strain}(\xi_{LP}, \xi_{TP},\ s_1, s_2) = E_{elastic}^{11} + E_{elastic}^{22} + E_{elastic}^{12} \tag{4}$$

All terms on the right-hand side are summed up with the elastic interaction energy between infinitesimal fractional dislocations derived from the cores of the partials, and they are calculated as:

$$
\begin{aligned}
E_{elastic}^{11} &= \int_{-\infty}^{\infty}\int_{-\infty}^{\infty}\left(\frac{K_{11}}{2\pi}\right)\rho_{LP}(x)\rho_{LP}(y)\ln|x-y|dxdy \\
E_{elastic}^{22} &= \int_{-\infty}^{\infty}\int_{-\infty}^{\infty}\left(\frac{K_{22}}{2\pi}\right)\rho_{TP}(x)\rho_{TP}(y)\ln|x-y|dxdy \\
E_{elastic}^{12} &= \int_{-\infty}^{\infty}\int_{-\infty}^{\infty}\left(\frac{K_{12}}{2\pi}\right)\rho_{LP}(x)\rho_{TP}(y)\left(\vec{b}_{LP}\cdot\vec{b}_{TP}\right)\ln|x-y|dxdy
\end{aligned}
\tag{5}
$$

where K_{11}, K_{22}, and K_{12} are the anisotropic interaction coefficients to be computed. As an example, the procedure to determine K_{12} can be briefly explained. We can consider the LP and TP separated by a certain distance R. The continuum strain-fields surrounding each Shockley partial are determined and superposed based on the E-S formalism to determine the net strain-field. The strain energy density is then numerically integrated to calculate the total strain-energy of interaction at the chosen separation distance R, and a core region within radius $5b_p$ around the center of each partial is excluded. By calculating the total strain-energy at varying R, the interaction coefficient K_{12} is determined. The choice of $5b_p$ does not affect K_{12} calculation since the gradient of change of total strain-energy is conserved. The self-interaction coefficients K_{11} and K_{22} can be similarly determined by considering the interaction between two dislocations with the same Burgers vectors of them. For more detailed exposition of anisotropic interaction coefficients and the E-S formalism, the reader is referred to elsewhere (Mohammed et al., 2022).

In order to formulate the misfit energy $E_{misfit}(\xi_{LP}, \xi_{TP}, s_1, s_2)$ of the extended dislocation, the generalized stacking fault energy (GSFE) curve is needed for each LP and TP. The GSFE curves for the LP and TP are represented as:

$$
\gamma_{LP}(u) = \begin{cases} \gamma_{isf} + \left(\frac{\gamma_{us}-\gamma_{isf}}{2}\right)\left(1-\cos\left(\frac{2\pi u}{b_P}\right)\right) & for\ 0 \le u \le \frac{b_P}{2} \\ \frac{\gamma_{us}}{2}\left(1-\cos\left(\frac{2\pi u}{b_P}\right)\right) & for\ \frac{b_P}{2} \le u \le b_P \end{cases}
\tag{6}
$$

$$
\gamma_{TP}(u) = \begin{cases} \frac{\gamma_{us}}{2}\left(1-\cos\left(\frac{2\pi u}{b_P}\right)\right) & for\ 0 \le u \le \frac{b_P}{2} \\ \gamma_{isf} + \left(\frac{\gamma_{us}-\gamma_{isf}}{2}\right)\left(1-\cos\left(\frac{2\pi u}{b_P}\right)\right) & for\ \frac{b_P}{2} \le u \le b_P \end{cases}
\tag{7}
$$

where γ_{us} and γ_{isf} are unstable and intrinsic stacking fault energies, respectively. Based on Eqns. (1), (2), and (6), (7), the total misfit energy E_{misfit} with the partitioned fault-energies for the individual Shockley partials can be rewritten as follows,

$$
E_{misfit}(\xi_{LP}, \xi_{TP}, s_1, s_2) = \frac{1}{L_{2D}}\left[\begin{array}{c} \sum_{n=-N_0}^{N_0}\sum_{m=-M_{max}}^{-1}\gamma_{TP}\left(f_{TP}\left(x_1^{(m,n)}\right)\right)\Delta A \\ \ldots\ldots + \sum_{n=-N_0}^{N_0}\sum_{m=0}^{M_{max}}\gamma_{LP}\left(f_{LP}\left(x_1^{(m,n)}\right)\right)\Delta A \end{array}\right]
\tag{8}
$$

where $x_1^{(m,n)} = (m\vec{a}_1 + n\vec{a}_2)\cdot\vec{e}_1$, ΔA is the area of the WS cell, and L_{2D} is the normalization length based on repeating dislocation lines. A summation limit of M_{max} is chosen with a large number, in the order of 10^4, to sufficiently converge the misfit energy $E_{misfit}(\xi_{LP}, \xi_{TP}, s_1, s_2)$. The misfit energy given by Eqn. (8) is calculated per unit length of the dislocation line. Consequently, four parameters (ξ_{LP}, ξ_{TP}, s_1, s_2) are determined based on the Eqn. (3) with respect to the equilibrium core-structure (ξ_{LP}^0, ξ_{TP}^0, s_1^0, s_2^0) at the ground state by minimizing E_{total}

$$
\frac{\partial E_{total}}{\partial \xi_{LP}} = 0; \quad \frac{\partial E_{total}}{\partial \xi_{TP}} = 0; \quad \frac{\partial E_{total}}{\partial s_1} = 0; \quad \frac{\partial E_{total}}{\partial s_2} = 0
\tag{9}
$$

The minimization routine is implemented with *fmincon* in MATLAB. Details for the dependence of each energy component on the core-parameters are found in the previous study (Mohammed et al., 2022). In the following sections, the equilibrium core-structure parameters (ξ_{LP}^0, ξ_{TP}^0, s_1^0, s_2^0) are used to determine the CRSS.

2.2. *Minimum energy path (MEP) and critical resolved shear stress (CRSS)*

In this work, the minimum energy path (MEP) is examined with the equilibrium core-widths (ξ_{LP}^0, ξ_{TP}^0) to find the triangular trajectory that allows the robust intermittent movement of Shockley partials but limits either trailing or leading partial while the other moves. Therefore, the triangular trajectory can be more energetically favorable than the Fourier-series that was proposed in the original work. The positions of Shockley partials (s_1, s_2) are described by the following equations along with the triangular trajectory,

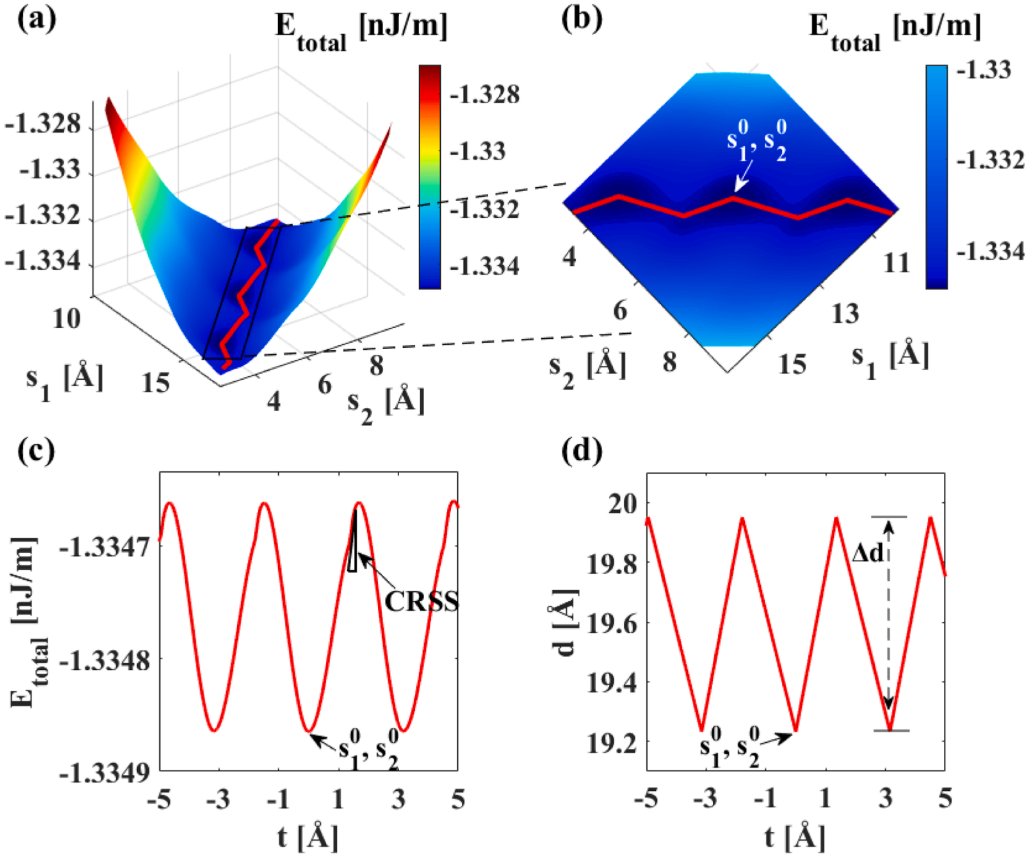

Fig. 2. The ab-initio calculation of Critical Resolved Shear Stress (CRSS) using set-up input parameters, (a) total energy landscape, and positions of Shockley partial dislocations. The minimum energy path (MEP), the zig-zag, is denoted as the red line, (b) the enlarged representation for the triangular MEP, the intermittent motion of partials is denoted. (c) the CRSS is calculated at the maximum slope of total energy along with the OET, (d) stacking fault width d is in the zig-zag motion with Δd. These are the results for one of hypothetical materials, which has ($a = 3.67$ Å, $C_{11} = 285$ GPa, $C_{12} = 155$ GPa, $C_{44} = 95$ GPa, $\gamma_{us} = 230$ mJ/m^2, $\gamma_{isf} = 105$ mJ/m^2).

$$
\begin{aligned}
s_1 &= s_1^0 + \frac{1}{\sqrt{2}}\left(t + \sum_{k=1}^{n} C_k\left(1 - P\left(C_p, j\right)\right)\right) \\
s_2 &= s_2^0 + \frac{1}{\sqrt{2}}\left(-t + \sum_{k=1}^{n} C_k\left(1 - P\left(C_p, j\right)\right)\right)
\end{aligned}
\tag{10}
$$

where t is a path variable to parametrize the trajectory. $P(C_p, j)$ is the triangular pulse generator and j is a pulse-variable, which are defined as,

$$
j = \frac{t}{C_q} + C_p - \left\lfloor \frac{t}{C_q} + C_p \right\rfloor
\tag{11}
$$

$$
P\left(C_p, j\right) = \begin{cases} 0 & \text{for } j \le 0 \\ \dfrac{j}{C_p} & \text{for } 0 < j < C_p \\ \dfrac{1 - j}{1 - C_p} & \text{for } C_p < j < 1 \\ 0 & \text{for } j \ge 1 \end{cases}
\tag{12}
$$

where the lower bracket of $\lfloor x \rfloor$ is a floor function $\lfloor x \rfloor . = \max\{X \in \mathbb{Z} : X \le x\}$, and the parameter combination $(C_1, \ldots, C_n, C_p, C_q)$ defines a shape for a triangular path of positions of Shockley partials. The cumulative total energy along with the path given in Eqn. (10) is accordingly defined as the following objective function,

Table I
Variable descriptions of parametric study on the CRSS for individual materials' fingerprints. As one parameter is varying, the others are fixed with the given values for simplicity. Corresponding results are depicted in Fig. 3.

Varying material constants	Fixed material constants			
Lattice constant, a	$\gamma_{us} = 230$ mJ/m^2	$\gamma_{isf} = 105$ mJ/m^2	$\mu = 65$ GPa	$C_{44} = 95$ GPa
Unstable stacking fault energy, γ_{us}	$a = 3.62$ Å	$\gamma_{isf} = 25$ mJ/m^2	$\mu = 65$ GPa	$C_{44} = 95$ GPa
Shear modulus, $\mu = (C_{11} - C_{12})/2$	$\gamma_{us} = 230$ mJ/m^2	$\gamma_{isf} = 105$ mJ/m^2	$a = 3.62$ Å	$C_{44} = 95$ GPa
Elastic modulus, C_{44}	$\gamma_{us} = 230$ mJ/m^2	$\gamma_{isf} = 105$ mJ/m^2	$a = 3.62$ Å	$\mu = 65$ GPa

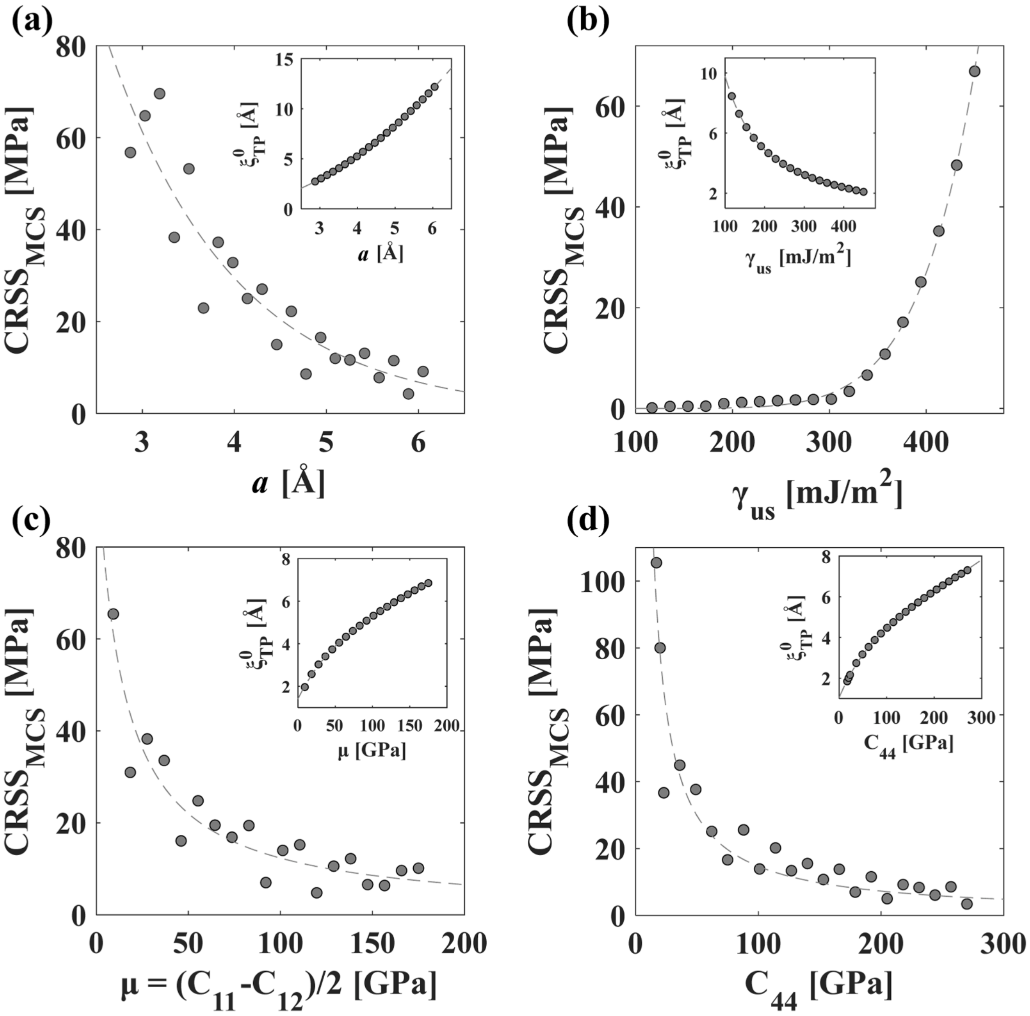

Fig. 3. Results of the CRSS based on the analytic MCS framework for each parameter of (a) lattice constant a, (b) unstable stacking fault energy γ_{us}, and the elastic moduli of (c) $\mu = (C_{11} - C_{12})/2$, and (d) C_{44}. Each inset figure represents the relation between each parameter and the corresponding equilibrium core-width of the trailing partial (ξ^0_{TP}).

$$E_{path}(C_1, \ldots, C_n, C_p, C_q) = \sum_i E_{total}\left(s_1(t_i), s_2(t_i), \xi^0_{LP}, \ \xi^0_{TP}\right) \tag{13}$$

The number of periodic functions is simply set to $n = 1$ sufficient to capture the MEP. The roles of path parameters such as t and (C_1,C_p, C_q) can be also understood with the equilibrium point found at $t = 0$ for (s_1^0,s_2^0) with $C_1 = 0$, which is the amplitude of triangular path. C_p and C_q are a peak position and a period of the triangular path, respectively. The triangular pulse generator $P(C_p, j)$ is demonstrated with *triangularPulse* in MATLAB. The equilibrium parameters (ξ^0_{LP}, ξ^0_{TP}, s_1^0, s_2^0) are employed along with the triangular trajectory described by Eqn. (10), and the minimization routine in Eqn. (13) is implemented with *fmincon* and multiple initial points (*MultiStart*) in MATLAB to find the corresponding MEP.

Conventionally, the CRSS has been calculated using Peierls-Nabarro (PN) model (Joós and Duesbery, 1997; Nabarro, 1947; Peierls, 1940), taking only the misfit-energy based on one-dimensional simple-cubic row-summation. Thus, it is expressed as,

$$CRSS_{PN} = \max\left(\frac{1}{b_F}\frac{dE^{PN}_{misfit}}{du}\right) \tag{14}$$

where b_F is the magnitude of the full dislocation, $E^{PN}_{misfit}(u) = \sum_{m=-\infty}^{\infty}\gamma(f(ma' - u))a'$, γ is the GSFE curve, f is the disregistry function given by equation x, and a' is interplanar spacing perpendicular to the dislocation line (i.e. along x_1 refer Fig. 1), respectively. However, the PN model has the following limitations in the determination of the CRSS within extended dislocations: (i) the individual Shockley partials are assumed to move simultaneously with a constant stacking fault width, (ii) the CRSS is assumed to be dependent on the full Burgers vector b_F only, not on the partial Burgers vector b_p, and (iii) solely misfit-energy is considered based on the one-dimensional simple-cubic row-summation. In this study, we adopt the optimum-energy-trajectory (OET) approach for the CRSS prediction that resolves these challenges in their entirety based on total energy $E_{total}(\xi_{LP},\xi_{TP}, s_1,s_2)$. For more detailed coverage of the OET approach and its derivation reader is referred to the original work suggested by Mohammed-Celebi-Sehitoglu (MCS) (Mohammed et al., 2022). Following this approach, the CRSS is computed as,

$$CRSS_{MCS} = SF_F \cdot \max\left(\frac{1}{(SF_{LP}\cdot s_1'(t) - SF_{TP}\cdot s_2'(t))}\frac{1}{b_p}\frac{dE_{total}}{dt}\right) \tag{15}$$

where b_p is the magnitude of the Burgers vector in Shockley partials, and $SF_F = (\vec{v}\cdot\vec{n}_{slip})(\vec{v}\cdot\vec{b}_F)$, $SF_{LP} = (\vec{v}\cdot\vec{n}_{slip})(\vec{v}\cdot\vec{b}_{LP})$, $SF_{TP} = (\vec{v}\cdot\vec{n}_{slip})(\vec{v}\cdot\vec{b}_{TP})$ are Schmid Factors (SFs) resolved in the full extended dislocation, leading, and trailing partials, $\vec{v}$ is the unit vector along uniaxial tensile load direction $[1\bar{3}2]$, and $\vec{n}_{slip} = 1/\sqrt{3}[1\bar{1}1]$ the normal vector to the slip plane, respectively.

Fig. 2 represents one example case obtained based on the framework with the triangular MEP described in Eqn. (10). The input parameters are set as $a = 3.67$ Å, $C_{11} = 285$ GPa, $C_{12} = 155$ GPa, $C_{44} = 95$ GPa, $\gamma_{us} = 230$ mJ/m^2, $\gamma_{isf} = 105$ mJ/m^2. In Fig. 2(a), the total energy contour, along with the positions of Shockley partials (s_1, s_2) is shown with the optimized MEP (red line). Based on the minimization in Eqn. (9), the equilibrium core-widths (ξ^0_{LP}, ξ^0_{TP}) of Shockley partials yield $\xi^0_{LP} = 5.86$ Å, $\xi^0_{TP} = 4.45$ Å, and their positions (s^0_1, s^0_2) are (13.1 Å, 6.18 Å) in Fig. 2(b), which results in the equilibrium stacking fault width $d_0 = 19.2$ Å. In Fig. 2(c), the total energy trajectory along with the MEP is plotted with respect to the path variable t. Then, the CRSS of the given input parameters finally yields the CRSS = 11.5 MPa based on Eqn. (15), at the maximum derivative of total energy, which is resolved in its OET. In Fig. 2(d), the intermittent zig-zag motion of Shockley partials implies a fluctuation in the stacking fault width during motion, $d = d_0 + \Delta d$, and the magnitude of this fluctuation for the present case is $\Delta d = 0.72$ Å as dictated by the input parameters. Especially, as the zig-zag stacking fault variations Δd are highlighted in our previous reference, it is in contrast to a common knowledge that the partials of the extended dislocation move together. We have the CRSS, core parameters (ξ^0_{LP}, ξ^0_{TP}), stacking fault widths d_0, and Δd as the outputs from the MCS framework with six material constants. In this study, we focus on the CRSS and how the material constants dictate it.

2.3. Parametric study on CRSS

To investigate the dependences of input parameters on the CRSS, we extend the range of study for each isolated parameter as the others are fixed as constants, which are tabulated in Table I. For material stability, the combinations of input parameters are ensured to have the conditions of i) $C_{11} > 0$; $C_{12} > 0$; $C_{44} > 0$, ii) $C_{11} > C_{12}$, and iii) $\gamma_{us} > \gamma_{isf}$, so that the simulated materials are theoretically plausible. Fig. 3 represents the CRSS with the four representative variables, including lattice constant a, unstable stacking-fault energy γ_{us}, and the moduli of $\mu = (C_{11} - C_{12})/2$ and C_{44}. In Fig. 3(a), the CRSS exponentially decreases as a increases, and the other hypothetical parameters are fixed as they are given in Table I. These hypothetical material constants are in the vicinity of the properties of real materials such as Ni and Cu (see Table S1 in Supplementary materials). In contrast, the CRSS exponentially increases as γ_{us} increases in Fig. 3(b). The other parameters are fixed as well similarly in Table I. For the elastic moduli, we vary μ and C_{44} instead of C_{11}, C_{12}, and C_{44}, respectively, in Fig. 3(c) and (d). In the variation of μ of Fig. 3(c), C_{44} is maintained as $C_{44} = 95$ GPa, whereas $\mu = 65$ GPa in Fig. 3 (d). The CRSS exponentially decreases as both moduli of μ and C_{44} increase. Each parametric dependence on the CRSS arises mainly from the variation of the core-widths of dislocation (inset figures), since the core-width of trailing partial (ξ^0_{TP}) oppositely varies in each case. The sensitivities of material constants show a comparable influence on the CRSS level (0~80 MPa) as each parameter changes. The variations in the CRSS have also uncertainties regarding each parameter, although they are dependent on the choice of the constants. The parametric study in this section is implemented with theoretically fixed other inputs to explore the individual propensities with the CRSS, although the properties of the practical materials are simultaneously changing in the complex interaction with each other. Therefore, the pool of input parameters is additionally needed to study randomness for the general prediction of the CRSS and the inverse design of novel FCC materials.

2.4. Data generation of hypothetical materials

To train the machine learning (ML) based prediction model of the CRSS, we generate the arbitrary combinations of six input parameters. The pool of input parameters is asserted to have the condition of material stability i) $C_{11} > 0$; $C_{12} > 0$; $C_{44} > 0$, ii) $C_{11} > C_{12}$,

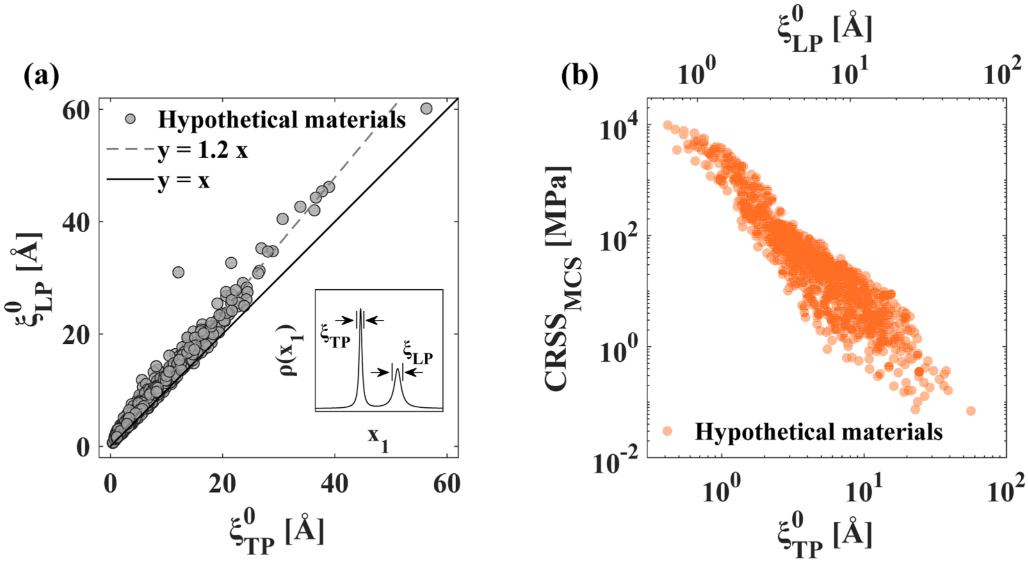

Fig. 4. Equilibrium core-widths and CRSS of hypothetical materials' fingerprints based on the MCS framework: (a) Core-widths of trailing versus leading partial (ξ^0_{TP}, ξ^0_{LP}), The schematic of dislocation density is depicted in the schematic inset. (b) the CRSS versus the core-widths of trailing (ξ^0_{TP}) and leading partial (ξ^0_{LP}) as a dual x-axis plot.

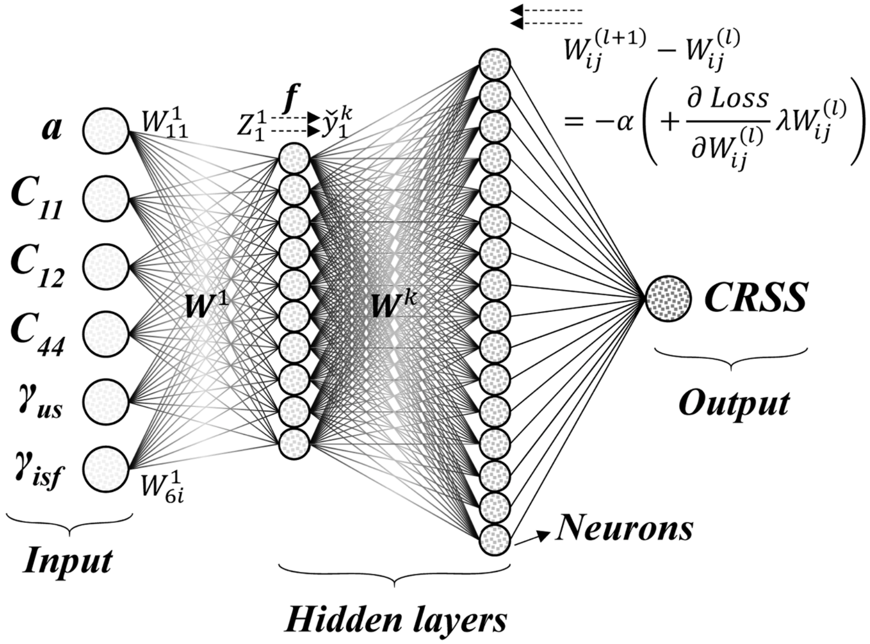

Fig. 5. Schematic of the Surrogate Neural Networks (SNN). The SNN consists of fully connected input, hidden, and output layers. The connections of the SNN include weights and biases to be optimized. A total of six materials' fingerprints (or features) feed the SNN model; lattice constant (a), three elastic constants (C_{11}, C_{12}, C_{44}), and unstable/intrinsic stacking fault energies (γ_{us}, γ_{isf}). The output layer is targeted to the CRSS. Calculus of neural networks is described in the text.

and iii) $\gamma_{us} > \gamma_{isf}$, but we also consider iv) positive intrinsic stacking-fault energy only in this work, i.e. $\gamma_{isf} > 0$, since the materials with the negative γ_{isf} have metastability (Li et al., 2014; Li et al., 2022; Werner et al., 2021). Each input parameter is randomly generated in the practical range of each property, and the pool of input stands for numerous hypothetical materials which may exist but remain unknown. The range of lattice constant a is set to 2.88 $\AA < a <$ 6.08 Å based on the list of a value of cubic metals in the periodic table (except Group 1 alkali metals). The range of elastic constants C_{11}, C_{12}, C_{44} is set to 80.5 GPa $< C_{11} <$ 599 GPa, 45.4 GPa $< C_{12} <$ 256 GPa, and 19.4 GPa $< C_{44} <$ 267 GPa based on the stability conditions and the values of cubic metals which are available in the

Table II
Ranges for searching hyperparameters of the SNN. All hyperparameters are set in the common ranges. The range of optimizer is set with stochastic gradient descent (SGD) and root mean squared propagation (RMSprop) with additional momentum variable (m), and adaptive moment estimation (Adam). All optimizers have a learning rate (α), and RMSprop and Adam have a Gamma decay variable (Γ).

The number of hidden layers	$1 \sim 10$
The number of neurons of each layer	$1 \sim 100$
Weight decay (λ) of each layer	$10^{-5} \sim 10^{-1}$
Optimizer	SGD(α, m) RMSprop(α, m, Γ) Adam(α, m, Γ)
Learning rate (α)	α: $10^{-5} \sim 10^{-1}$
Momentum (m)	m: $0.85 \sim 0.99$
Gamma decay (Γ)	Γ: $0.85 \sim 0.99$

literature (Simmons and Wang, 1971; Söderlind et al., 1993; Wills et al., 1992). The stacking-fault energies are less available with the number of reported data (Alkan et al., 2018; Celebi et al., 2022a; Kibey et al., 2007), and we have $81.3\ \mathrm{mJ/m^2} < \gamma_{\mathrm{us}} < 450\ \mathrm{mJ/m^2}$, and $2.1\ \mathrm{mJ/m^2} < \gamma_{\mathrm{isf}} < 330\ \mathrm{mJ/m^2}$. The pool of input parameters of hypothetical materials is made of 1000 sets, randomly chosen from each parameter's range above. The distributions of input data pool are represented within each parameter in Appendix A in Fig. A1. We acquired 976 results from them, including the CRSS, the equilibrium core-widths, and the MEP of Shockley partials using the MCS framework. This pool of 976 hypothetical materials data is represented in Table S2 in Supplementary Materials and applied to train the ML model in Section 2.5.

Fig. 4 represents the correlations between the equilibrium core-widths (ξ^0_{TP}, ξ^0_{LP}) and the CRSS of 976 fingerprints of hypothetical materials made of random input parameters. In Fig. 4(a), all the core widths of leading partial (ξ^0_{LP}) are larger by 1.2 times on average than the ones of trailing partial (ξ^0_{TP}), which recalls the non-symmetricity of the core-widths for mixed dislocation dissociation (see inset figure). It stems from the non-symmetric strain fields of the LP and TP due to the cubic anisotropy and the character of the dislocations. In Fig. 4(b), the CRSS corresponding to ξ^0_{TP} of hypothetical materials are represented. The CRSS exponentially changes in general as ξ^0_{TP} varies, but the deviations are found at the low-to-middle level of the CRSS. This may come from the non-symmetricity of core structures in the mixed dislocation character. For 60° mixed dislocation, the difference between ξ^0_{TP} and ξ^0_{LP} becomes larger as ξ^0_{TP} increases. Therefore, using the MCS framework, we generate a number of the CRSS data that hold the non-symmetric character of 60° mixed dislocation.

2.5. *Surrogate Neural Networks (SNN)*

In this work, we use the ML approach to model the CRSS of FCC materials with neural networks based on the MCS framework. Total 976 data of hypothetical materials' fingerprints and their CRSS are applied to the Surrogate Neural Networks (SNN). In this step, the SNN model is optimized using its hyperparameters. In Fig. 5, the schematic of the SNN is illustrated. The input layer consists of the six material's fingerprints (a, C_{11}, C_{12}, C_{44}, γ_{us}, and γ_{isf}) into each numerical neuron (node). Each layer is fully connected to the other with the corresponding number of neurons, which have initial weights and activation functions to calculate the numeric in the next layer. Then, all the hidden layers and the output layer repeat this calculation in the forward direction. Details of the general neural networks can be found elsewhere (Goodfellow et al., 2016; Krose and Smagt, 2011; Müller et al., 1995), and we summarize the calculus of neural networks here. The forward propagation of the numeric can be represented as,

$$z^k = W^k \hat{y}^{k-1} + b^k \tag{16}$$

where W^k is weight tensor, b^k bias vector, z^k intermediate output in a layer k, respectively. $\hat{y}$ can be regarded as the output from previous layer (k-1) or the input of current layer (k), which is transformed by activation function (f) based on the intermediate output (z^k) as follows,

$$\hat{y}^k = f^k\left(z^k\right) \tag{17}$$

and the final output layer calculates a loss (error) between prediction and ground truth for the target such as the CRSS. Based on the loss, all the layers adjust back W^k and b^k between their neurons. Then, this back-propagation can be established as,

$$W_{ij}^{(l+1)} - W_{ij}^{(l)} = -\alpha\left(\frac{\partial Loss}{\partial W_{ij}^{(l)}} + \lambda W_{ij}^{(l)}\right) \tag{18}$$

$$b_i^{(l+1)} - b_i^{(l)} = -\alpha\left(\frac{\partial Loss}{\partial b_i^{(l)}} + \lambda b_i^{(l)}\right) \tag{19}$$

Table III
Hyperparameters for the optimized SNN. The number of neurons and weight decays (λ) are tabulated in each row.

The number of hidden layers	4
1st hidden layer	84, λ=2.67×10^{-5}
2nd hidden layer	45, λ=7.67×10^{-2}
3rd hidden layer	60, λ=1.46×10^{-5}
4th hidden layer	91, λ=1.49×10^{-3}
Output layer	1, λ=1.30×10^{-4}
Optimizer	RMSprop(α, m, Γ)
Learning rate (α)	α: 2.41×10^{-4}
Momentum (m)	m: 0.89
Gamma decay (Γ)	Γ: 0.96

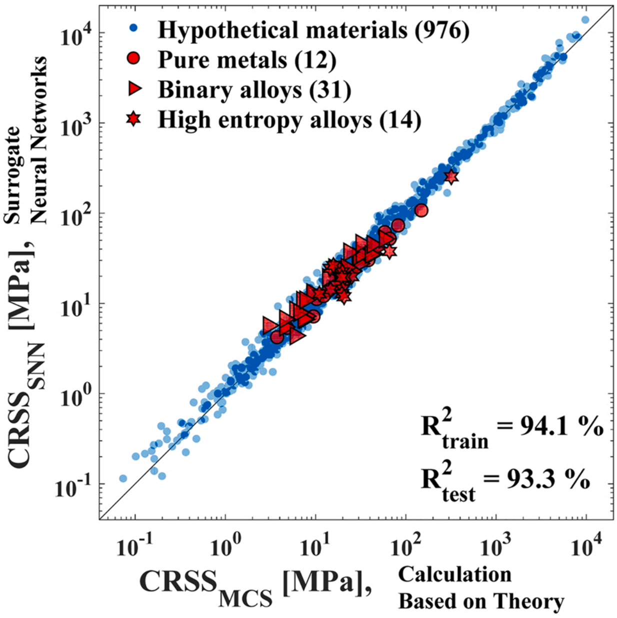

Fig. 6. Prediction of CRSS using the optimized SNN model; CRSS of the SNN prediction versus the raw data from the MCS framework. Hypothetical materials are used in training the SNN, and known materials are test datasets (red) including FCC pure metals, binary, and high entropy alloys.

where α is learning rate, and *Loss* is loss function to be defined, respectively. The weights $W_{ij}^{(l)}$ and biases $b_i^{(l)}$ in the number of neurons in previous (i) and current layer (j) are updated in an iteration l. In this work, we apply weight decay (λ), which is a regularization variable to better balance the model between overfitting and underfitting (Krogh and Hertz, 1992). Then, these whole forward- and back-propagations (double arrows in Fig. 5) are implemented in repetition for the given number of epoch(s).

The SNN is then optimized with respect to the weights using hyperparameters such as the number of hidden layers, the number of neurons and weight decay (λ) of each layer, and optimizer and its variables. In this work, we search for the best optimizer among stochastic gradient descent (SGD), root mean squared propagation (RMSprop), and adaptive moment estimation (Adam). Details of the optimizers' algorithms can be found elsewhere (Goodfellow et al., 2016). They have a common variable of learning rate (α), which is crucial to balance fitting losses. The other optimizers and their additional variables stand for adaptive modulation of α. RMSprop and Adam have a gamma decay (Γ) that manipulates a moving average in gradients of the *Loss* by rescaling α. Adam has also a momentum (m) controller that can accelerate the minimization by considering past gradients of the *Loss*. SGD and RMSprop are also combined with m in this work. Although common ranges of these hyperparameters have been studied well, the best choice of them in different problems remains an empiricism. Therefore, we search for the optimum hyperparameters in the range given in Table II. The SNN models in the searching loops were constructed using the Keras and TensorFlow (Abadi et al., 2016; Chollet, 2015). We optimized the hyperparameters of the SNN models using the Optuna (Akiba et al., 2019). The activation functions for the hidden and output layers are respectively defined as the rectified linear (ReLU) and linear units. The output loss function is chosen as mean-squared-error (MSE) described in the following equation,

$$Loss = \frac{1}{N}\sum_{r=1}^{N}(y_r - \widehat{y}_r)^2 \tag{20}$$

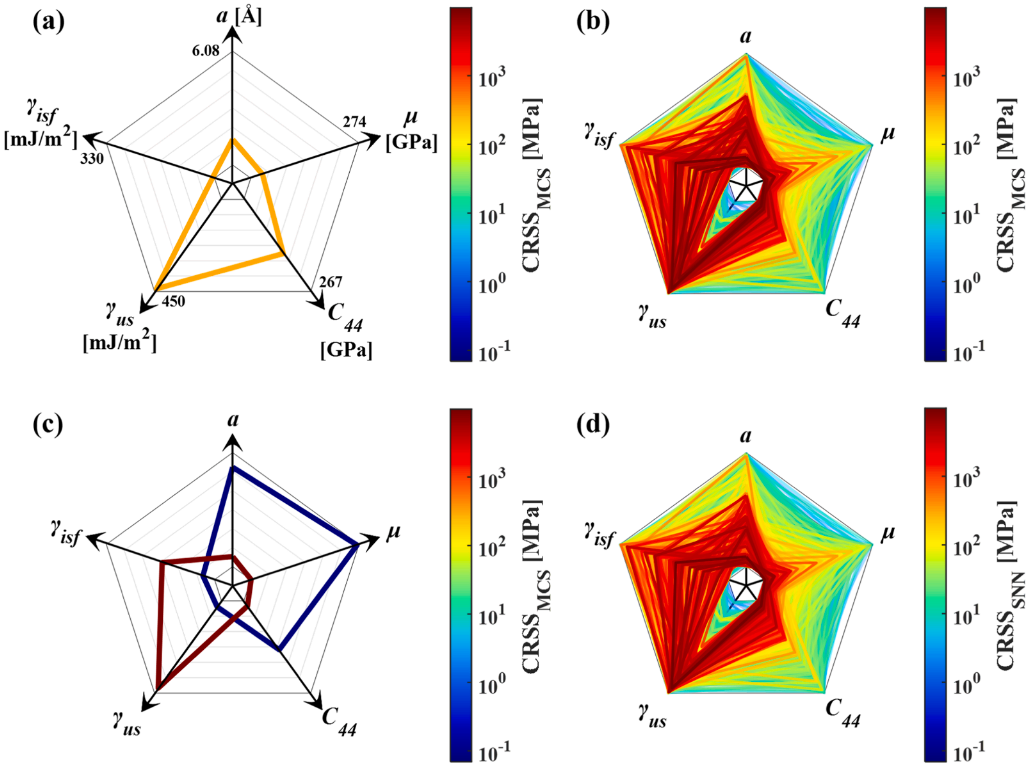

Fig. 7. (a) 5-axis spider-chart representation of a single material's "fingerprint" that consists of five continuum-atomistic properties: (*a*, μ, C_{44}, γ_{us}, and γ_{isf}); From the innermost to outermost regular pentagon, *a* varies from 2.88 Å to 6.08 Å, μ from 5.05 GPa to 274 GPa, C_{44} from 19.4 GPa to 267 GPa, γ_{us} from 81.3 mJ/m^2 to 450 mJ/m^2, and γ_{isf} from 2.10 mJ/m^2 to 330 mJ/m^2. Tick of each axis is linearly spaced by gray regular pentagons with *a* (0.53 Å), μ (44.9 GPa), C_{44} (41.3 GPa), γ_{us} (61.4 mJ/m^2), and γ_{isf} (54.7 mJ/m^2); each material can be represented as a pentagon in this 5-axis chart and the pentagon is color-coded with the predicted-CRSS corresponding to this fingerprint; the most inner and outer pentagons are respectively the minimum and maximum of each property; a plot of FeNiCoCrMn with ($a = 3.6$ Å, $\mu = 34.5$ GPa, $C_{44} = 165$ GPa, $\gamma_{us} = 439$ mJ/m^2, and $\gamma_{isf} = 8$ mJ/m^2) is shown. (b) Plot of the complete dataset generated from predictions of analytical MCS model (contains 1033 material-property fingerprints and the corresponding CRSS). (c) Plot of material fingerprints (alluded to in the main text) exhibiting the highest and the lowest CRSS predictions from the analytical MCS model. (d) Plot generated from SNN predictions (including all 1033 fingerprints from (c)); the developed SNN model captures the predicted behavior from the analytical MCS model.

where *N* is the number of data, $\widehat{y}_r$ and y_r are the predictions and ground truths for the target. The target output in the SNN modeling is logarithmically scaled to consider the wide range of the CRSS ($10^{-2} \sim 10^4$ MPa). A total of 976 data are divided into training (90%, 878) and validation sets (10%, 98), and the losses for both sets are recorded. Here, the training set is utilized to minimize the *Loss* and thus update W^k and b^k in each epoch. The validation set is not used for the update but is utilized to evaluate the model in each epoch. It has different input and output data split by 10% from the total set, so the *Loss* of the validation set at the final epoch is used to search for the SNN as the optimum. The optimum hyperparameters are selected at which the lowest validation *Loss* has been found. Within 1000 epochs as the maximum for all searching trials (300), the hyperparameters of the optimized SNN are constructed in Table III. Its convergence of the MSE loss has been also monitored as depicted in Fig. B1 of Appendix B. Based on the optimum SNN, therefore, we investigate its performance of predictions.

Fig. 6 represents the predictions of CRSS based on the optimized SNN. We calculate the accuracies of the SNN predictions based on the coefficient of determination (R^2), which is defined as,

$$R^2 = 1 - \frac{\sum_{r=1}^{N} (y_r - \widehat{y}_r)^2}{\sum_{r=1}^{N} (y_r - \overline{y})^2} \tag{21}$$

where $\overline{y}$ is the average of ground truths for the CRSS. A total of 976 hypothetical FCC materials are inherent in the SNN model with 94.1% of high accuracy. The ground truths and SNN predictions of the CRSS are tabulated in Table S2 in Supplementary Materials. However, it may not be generalizable for numerous real unknown materials. In this work, we implement the evaluation of the SNN with a test set, which has independence from training and validation sets (hypothetical materials - 976). In order to test and generalize the SNN into real materials, we acquired fingerprints of numerous FCC metals and alloys whose all six input parameters may be compatibly available. Total 57 FCC samples, including 12 pure metals (Collard and McLellan, 1992; Kibey et al., 2007; Neighbours and

Smith, 1954; Simmons and Wang, 1971), 31 binary alloys (Bandyopadhyay and Gupta, 1977; Celebi et al., 2022a; Leamy and Warlimont, 1970; Li et al., 2014; Siegel, 2005), and 14 high entropy alloys (Li et al., 2022), were investigated and solved into the analytic MCS framework to compare to their predictions. Some pure metals have different reported unstable/intrinsic stacking fault energies (γ_{us}, γ_{isf}) (Li et al., 2014). However, both the MCS and SNN models can yield different CRSS levels that correspond to different γ_{us} and γ_{isf}. It implies that both the MCS and SNN models can encompass the discrepancies over the same materials by users. Each accuracy on a different FCC class is listed in Table S3 in Supplementary Materials, and the overall accuracy is 93.3% on the test datasets of all FCC metals and alloys. This indicates the high resolution of prediction of the CRSS in general FCC materials via the SNN.

3. Discussion

The current study demonstrates three points: 1) the availability of a large data acquisition of the CRSS as well as the parameters of core structures such as ξ^0_{LP}, ξ^0_{TP}, and stacking-fault widths d_0, and Δd from the novel ab-initio CRSS framework which have not yet been found elsewhere, 2) the characteristics of which the combinations of materials' fingerprints dictate the CRSS, and 3) the SNN model that can rapidly predict the CRSS and have similar implications of their characteristics from the theory. The existing studies have mainly demonstrated limited experimental or theoretical analyses for the CRSS and the mixed characters of dislocation slips. Based on the analytic MCS framework, we showed the advancements in the CRSS as well as the properties of core structures (ξ^0_{LP}, ξ^0_{TP}), the stacking-fault widths d_0, and their variations Δd in the mixed character of dislocation. Especially, using hypothetically random combinations of the fingerprints, we also found the magnitude of non-symmetricity of the equilibrium core-widths and the relationship between the core-widths and the CRSS in Fig. 4. This may state the general characteristics of the mixed dislocation slip in FCC materials. Further calculations in the different mixed characters are available within the MCS framework.

With a large dataset of hypothetical materials' fingerprints, we can also narrow down the combinations of the characteristics that strongly dictate the CRSS. In Fig. 7, we illustrate the spider charts that consist of 5-axis with respect to five materials' fingerprints (a, μ, C_{44}, γ_{us}, and γ_{isf}). Thus, each material can be represented as a pentagon in this 5-axis chart, and the pentagon is color-coded with the CRSS corresponding to its fingerprint. In Fig. 7(a), a middle level of CRSS and its material's fingerprint are depicted for one of the high entropy alloys (HEAs), FeNiCoCrMn. Its CRSS is 318.4 MPa based on the analytic MCS framework, and it has low lattice constant (a), shear modulus (μ), intrinsic stacking fault energy (γ_{isf}), and high unstable stacking fault energy (γ_{us}), as each value is alluded to in figure. Fig. 7(b) and (c) can explain more details on the characteristics of the level of the CRSS. In Fig. 7(b), the CRSS (colors of pentagons) increases with low a, μ, and C_{44}, and high γ_{us}. This is a similar trend verified with the simple combinations of parameters by varying only 1 parameter at a time in Fig. 3, and we identify it in an extended large dataset with random hypothetical materials as well as real ones. These distinct correlations between the CRSS and a, μ, and C_{44} are uncovered in this work, while the dependence of only γ_{us} was known in general. Based on the parametric study in Fig. 3, we can deduce that the dependencies of a, μ, and C_{44} on the CRSS stem from the equilibrium core-widths (ξ^0_{LP}, ξ^0_{TP}). Specifically, the decreases in the elastic moduli μ and C_{44} result in a narrower ξ^0_{LP} and ξ^0_{TP}, which are mediated by the strain energy between two partials and the misfit energy of the lattice slip plane. The lower elastic moduli increase the repulsive strain energies in the interaction of two partials while they decrease the misfit energies, and hence the dislocation cores become narrowly concentrated. The dependency of a on the CRSS is also similarly related to ξ^0_{LP} and ξ^0_{TP}, but a can derive the higher or lower repulsive strain energies in the interactions of two partials and misfit energies by a differently being spaced. Then, this would correspondingly change ξ^0_{LP} and ξ^0_{TP}. With respect to γ_{us}, its dependency has been clear that its increase results in a higher energy barrier to move the dislocation slip, which dictates the higher CRSS. The findings in this work also suggest the effect of the narrower ξ^0_{LP} and ξ^0_{TP} underlying behind this correlation.

The maximum (the reddest pentagon) and minimum (the bluest) CRSS and their fingerprints are depicted in Fig. 7(c). The extremely low and high levels of CRSS are mostly covered with hypothetical materials. The maximum CRSS is 9755 MPa with a hypothetical fingerprint of $a = 3.16$ Å, $\mu = 5.80$ GPa, $C_{44} = 32.9$ GPa, $\gamma_{us} = 430$ mJ/m^2, and $\gamma_{isf} = 161$ mJ/m^2, while the minimum CRSS is 0.0694 MPa with a hypothetical one of $a = 5.67$ Å, $\mu = 270$ GPa, $C_{44} = 150$ GPa, $\gamma_{us} = 105$ mJ/m^2, and $\gamma_{isf} = 37.6$ mJ/m^2. Therefore, the HEA FeNiCoCrMn is at the middle level of CRSS in the given scale since it has low a, μ, and high γ_{us}, but high C_{44}, which generally reduces the CRSS. Based on the consideration of the core-structures, the hypothetical material with the maximum CRSS and the HEA FeNiCoCrMn have much narrower ξ^0_{LP} and ξ^0_{TP} (0.632 Å, 0.418 Å) and (2.96 Å, 2.10 Å), respectively, rather than the one with the minimum CRSS (60.1 Å, 56.3 Å). Therefore, the core-widths ξ^0_{LP} and ξ^0_{TP} mediated CRSS behavior is confirmed with the reduced materials' fingerprints. Also, because of the widely selected fingerprints in randomness, the characteristics of their combinations dictating CRSS may also hold for the general FCC materials. Hence, this analysis can stand for the inverse design of the CRSS in large compositional ranges of novel FCC materials.

For the rapid prediction of the CRSS, which is almost instant after learning, we showed the optimized SNN in the high accuracies in Fig. 6. This is comparative with the analytic MCS framework itself mostly taking hours at every single material, because of its low tolerance and manual validity of the MEP of Shockley partials. In Fig. 7(d), we also represent the spider-chart of the SNN predictions of CRSS with respect to five fingerprints. In this high-dimensional space, the SNN covers well the characteristics that come originally from the analytic MCS framework. It is also given the higher CRSS with the combinations of low a, μ, and C_{44}, and high γ_{us}. Therefore, with the purpose of the design of mechanics and materials for the CRSS in FCC materials, the SNN model can readily guide us to investigate the material's fingerprints corresponding to the target CRSS without heavy computations. To design the CRSS higher than the HEA FeNiCoCrMn (318.4 MPa), for instance, one may expect numerous potential materials with smaller a, μ, and/or C_{44} based on the spider-chart without any sophisticated consideration of the core-widths, and the strain and misfit energies. They can be experimentally tailored even with small changes in solute concentration in FeNiCoCrMn (Tian et al., 2013). Then, one can instantaneously guess their accurate CRSS using the SNN rather than the analytic framework. With the properly trained SNN providing instant forward functional evaluations, uncertainty quantification and sensitivity analysis can be studied as well in the future. We note that the SNN in this study aims at the CRSS only as an output for a simple purpose. One may further extend the procedures to the parameters of core structures ξ_{LP}^{0}, and ξ_{TP}^{0}, and stacking-fault widths d_0, and Δd with various mixed characters of dislocation slips. It is also a worthwhile work in the future to apply the similar approach combined with the modified MCS frameworks such as for both HCP and FCC materials and for low-to-finite temperatures.

4. Conclusion

In conclusion, the current study demonstrates a machine learning (ML) model of critical resolved shear stress (CRSS) of mixed dislocation slip based on a large dataset acquired from novel ab-initio frameworks. The following conclusions are drawn from the study:

a Triangular trajectories describe that the intermittent motions of dislocations occur for all materials. Their minimum energy paths (MEPs) give us a clear zig-zag nature of leading and trailing of Shockley partials movement, and therefore the stacking fault width variations. Depending on the material constants, the amplitude of zig-zag can be largely varied.

b A large dataset has been constructed using the analytic frameworks, including more than 1000 of the CRSS and the corresponding materials' fingerprints such as lattice constant a, unstable/intrinsic stacking-fault energies γ_{us}, γ_{isf}, and three elastic moduli C_{11}, C_{12}, and C_{44}. Dataset comprises hypothetically random combinations of the materials' fingerprints, and it may generally rule out the characteristics of dislocation slips in FCC materials.

c Dataset also has the other outputs of equilibrium core widths for leading and trailing partials (ξ_{LP}^{0}, ξ_{TP}^{0}), and equilibrium stacking-fault widths d_0, and their variations Δd in the triangular MEPs. The parameters of the equilibrium states have been determined with respect to the total energy landscape in the ab-initio frameworks. The similar procedure to this study can be further extended to these parameters as well.

d The core-widths (ξ_{LP}^{0}, ξ_{TP}^{0}) of Shockley partials have non-symmetricity that ξ_{LP}^{0} is generally larger by 1.2 times than ξ_{TP}^{0}, since the non-symmetric strain fields result from the cubic anisotropy and the mixed character of dislocation. The CRSS exponentially decreases as the ξ_{TP}^{0} increases, but it scatters in the low-middle level of the CRSS, probably because of the non-symmetricity of the core widths.

e ML-based Surrogate Neural Networks (SNN) have been modeled to readily predict the CRSS. The SNN is trained with a large dataset of hypothetical materials (976) and optimized using multiple hyperparameters. The optimized SNN is then tested with the real materials (57), including pure metals, binary, and high entropy alloys (HEAs). The SNN results in high accuracies on both hypothetical (94.1%) and real materials (93.3%).

f The CRSS exponentially increases as a, shear modulus $\mu = (C_{11}$ - $C_{12})/2$, and C_{44} decrease and/or γ_{us} increases for general FCC materials. These correlations are mediated by the change of (ξ_{LP}^{0}, ξ_{TP}^{0}) and it stems from the changes of repulsive strain energy and misfit energy. The real materials, including the HEAs such as FeNiCoCrMn, are at the middle level of CRSS with the range of $10^1 \sim 10^2$ MPa. These characteristics are precisely demonstrated in the optimized SNN without any calculations of core-widths and energies.

CRediT authorship contribution statement

Daegun You: Methodology, Investigation, Software, Formal analysis, Validation, Writing – original draft, Writing – review & editing, Visualization. **Orcun Koray Celebi:** Conceptualization, Methodology, Software, Investigation, Writing – original draft, Writing – review & editing, Supervision. **Ahmed Sameer Khan Mohammed:** Conceptualization, Methodology, Software, Investigation, Writing – original draft, Writing – review & editing, Supervision. **Diab W. Abueidda:** Supervision, Investigation, Writing – review & editing. **Seid Koric:** Resources, Supervision, Investigation, Writing – review & editing, Project administration, Funding acquisition. **Huseyin Sehitoglu:** Conceptualization, Investigation, Supervision, Project administration, Funding acquisition, Writing – review & editing.

Declaration of Competing Interest

The authors declare that they have no known competing financial interests or personal relationships that could have appeared to influence the work reported in this paper.

Data availability

Data will be made available on request.

Acknowledgment

We note that D. You and O. K. Celebi contributed equally to this paper. The work is supported by the National Science Foundation (NSF) under award number CMMI-21-25821, which is gratefully acknowledged. The use of the Illinois Campus Cluster, a computing resource that is operated by the Illinois Campus Cluster Program (ICCP) in conjunction with the National Center for Supercomputing Applications (NCSA) and which is supported by funds from the University of Illinois at Urbana-Champaign, is also gratefully acknowledged.

Supplementary materials

Supplementary material associated with this article can be found, in the online version, at doi:10.1016/j.ijplas.2023.103524.

Appendix A. Input data pool of hypothetical materials

The pool of input parameters has the condition of material stability i) $C_{11} > 0$; $C_{12} > 0$; $C_{44} > 0$, ii) $C_{11} > C_{12}$, iii) $\gamma_{us} > \gamma_{isf}$, and iv) positive intrinsic stacking-fault energy $\gamma_{isf} > 0$. Each input parameter is randomly generated in the practical range of each property, and the pool of input stands for numerous hypothetical materials which may exist but remain unknown. In Fig. A1, the range of lattice constant a is set to 2.88 $\mathring{A} < a <$ 6.08 Å, elastic constants C_{11}, C_{12}, C_{44} to 80.5 GPa $< C_{11} <$ 599 GPa, 45.4 GPa $< C_{12} <$ 256 GPa, and 19.4 GPa $< C_{44} <$ 267 GPa, and stacking-fault energies γ_{us}, γ_{isf} to 81.3 mJ/m$^2 < \gamma_{us} <$ 450 mJ/m^2, and 2.1 mJ/m$^2 < \gamma_{isf} <$ 330 mJ/m^2. The pool of input parameters of hypothetical materials is made of 1000 sets, but we acquired 976 results out of them, including the CRSS, the equilibrium core-widths, and the OET of Shockley partials using the MCS framework.

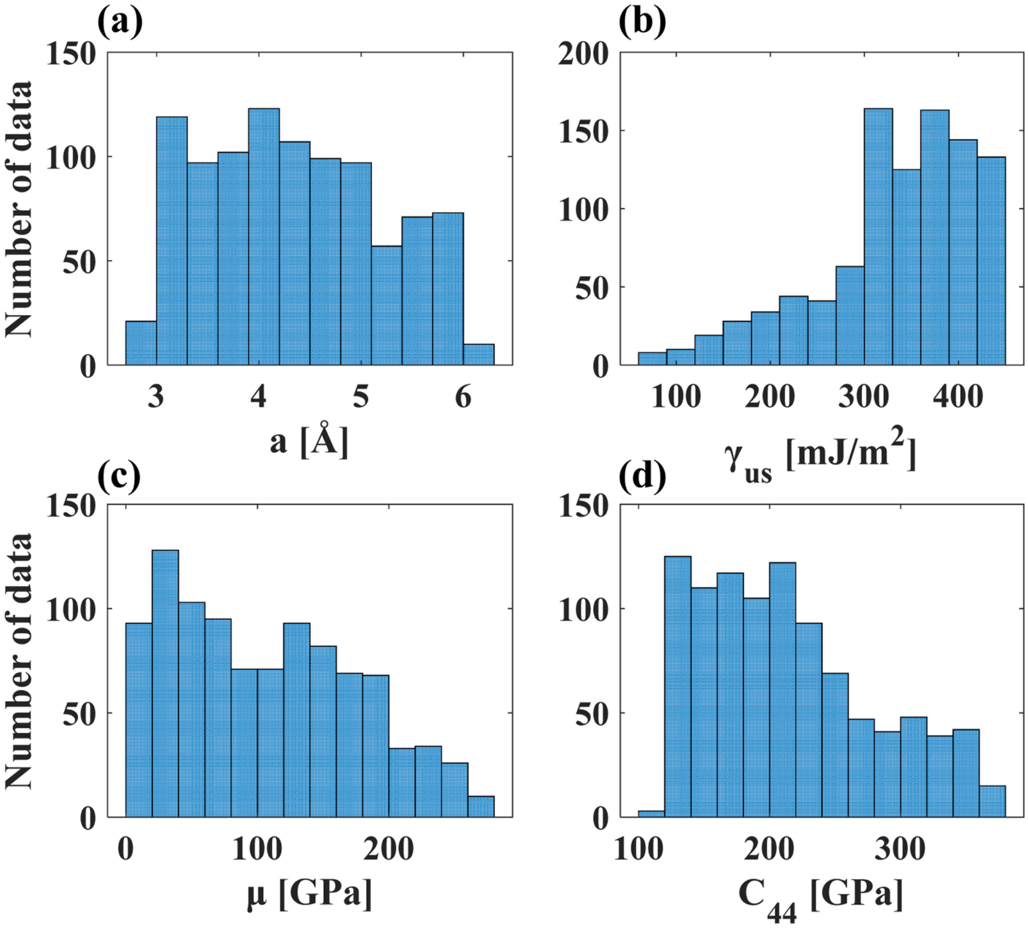

Fig. A1. Number of data distributions of input parameters used for the CRSS of hypothetical materials; (a) lattice constant, a, (b) unstable stacking fault energy, γ_{us}, (c) shear modulus, $\mu = (C_{11} - C_{12})/2$, (d) elastic modulus, C_{44}.

Appendix B. Convergence of loss function of neural networks

With the maximum searching iterations (300) for the ranges of hyperparameters tabulated in Table I, the optimum hyperparameters are selected at which the lowest validation *Loss* has been found using the Optuna (Akiba et al., 2019). Within the maximum 1000 epochs for all searching iterations, the hyperparameters of the optimized SNN are tabulated in Table III. Fig. B1 represents the convergence of the MSE losses that are normalized by $\frac{1}{N}\sum_{r=1}^{N}(y_r-\bar{y}_r)^2$ where $\bar{y}_r$ is the average of ground truth. The normalized MSE loss will be reduced to the form of $\frac{\sum_1^N (y_r-\hat{y}_r)^2}{\sum_1^N (y_r-\bar{y}_r)^2}$ as a unit less feature. A total of 976 data are divided into training (90%, 878) and validation sets (10%, 98), and the losses for both sets are recorded. At the final state of learning, the SNN has 1.17%, and 2.19% of training and validation errors. This means the SNN may have less amount of errors in hypothetical materials and potentially unknown data. Therefore, the optimized SNN has been balanced well between overfitting and underfitting.

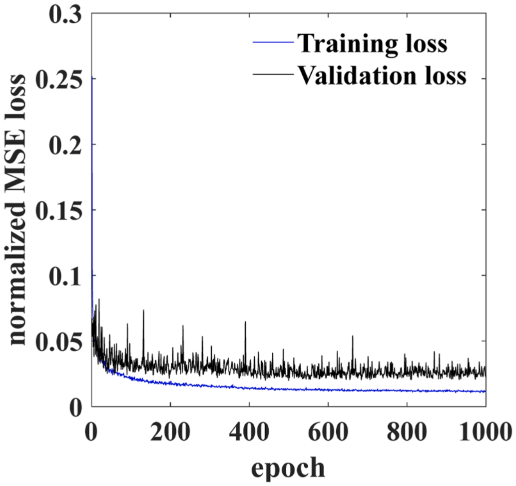

Fig. B1. Normalized loss function convergences for training and validation. Loss histories are obtained from the RMSprop optimizer based on the hyperparameters tabulated in Table III of the main text.

References

Abadi, M., Agarwal, A., Barham, P., Brevdo, E., Chen, Z., Citro, C., Corrado, G.S., Davis, A., Dean, J., Devin, M., 2016. Tensorflow: large-scale machine learning on heterogeneous distributed systems. arXiv preprint arXiv:1603.04467.

Abueidda, D.W., Koric, S., Al-Rub, R.A., Parrott, C.M., James, K.A., Sobh, N.A., 2022. A deep learning energy method for hyperelasticity and viscoelasticity. Eur. J. Mech. A Solids 95, 104639.

Abueidda, D.W., Koric, S., Sobh, N.A., Sehitoglu, H., 2021a. Deep learning for plasticity and thermo-viscoplasticity. Int. J. Plast. 136, 102852.

Abueidda, D.W., Lu, Q., Koric, S., 2021b. Meshless physics-informed deep learning method for three-dimensional solid mechanics. Int. J. Numer. Methods Eng. 122, 7182–7201.

Akiba, T., Sano, S., Yanase, T., Ohta, T., Koyama, M., 2019. Optuna: a next-generation hyperparameter optimization framework. In: Proceedings of the 25th ACM SIGKDD International Conference on Knowledge Discovery & Data Mining. Association for Computing Machinery. Anchorage, AK, USA, pp. 2623–2631.

Alkan, S., Ojha, A., Sehitoglu, H., 2018. Determination of latent hardening response for FeNiCoCrMn for twin-twin interactions. Acta Mater. 147, 149–164.

Argon, A., 2007. Strengthening Mechanisms in Crystal Plasticity. Oxford University Press.

Bandyopadhyay, J., Gupta, K.P., 1977. Low temperature lattice parameter of nickel and some nickel-cobalt alloys and Grüneisen parameter of nickel. Cryogenics (Guildf) 17, 345–347.

Barnett, D.M., Lothe, J., 1974. An image force theorem for dislocations in anisotropic bicrystals. J. Phys. F 4, 1618–1635.

Brenne, F., Mohammed, A.S.K., Sehitoglu, H., 2020. High resolution atomic scale characterization of dislocations in high entropy alloys: critical assessment of template matching and geometric phase analysis. Ultramicroscopy 219, 113134.

Celebi, O.K., Mohammed, A.S.K., Krogstad, J.A., Sehitoglu, H., 2022a. Evolving dislocation cores at twin boundaries: theory of CRSS elevation. Int. J. Plast. 148, 103141.

Celebi, O.K., Mohammed, A.S.K., Sehitoglu, H., 2022b. Dislocation Character Effect on CRSS in the Extreme. (submitted for publication).

Chollet, F., 2015. keras.

Chowdhury, P., Sehitoglu, H., Abuzaid, W., Maier, H.J., 2015. Mechanical response of low stacking fault energy Co–Ni alloys—continuum, mesoscopic and atomic level treatments. Int. J. Plast. 71, 32–61.

Collard, S.M., McLellan, R.B., 1992. High-temperature elastic constants of platinum single crystals. Acta Metall. Mater. 40, 699–702.

Gengor, G., Mohammed, A.S.K., Sehitoglu, H., 2021. $\{10\bar{1}2\}$ Twin interface structure and energetics in HCP materials. Acta Mater. 219, 117256.

Goli, E., Vyas, S., Koric, S., Sobh, N., Geubelle, P.H., 2020. ChemNet: a deep neural network for advanced composites manufacturing. J. Phys. Chem. B 124, 9428–9437.

Goodfellow, I., Bengio, Y., Courville, A., 2016. Deep Learning. MIT press.

Guo, Y., Cao, X., Liu, B., Gao, M., 2020. Solving partial differential equations using deep learning and physical constraints. Appl. Sci. 10, 5917.

Joós, B., Duesbery, M.S., 1997. The Peierls stress of dislocations: an analytic formula. Phys. Rev. Lett. 78, 266–269.

Kibey, S., Liu, J.B., Curtis, M.J., Johnson, D.D., Sehitoglu, H., 2006. Effect of nitrogen on generalized stacking fault energy and stacking fault widths in high nitrogen steels. Acta Mater. 54, 2991–3001.

Kibey, S., Liu, J.B., Johnson, D.D., Sehitoglu, H., 2007. Predicting twinning stress in fcc metals: linking twin-energy pathways to twin nucleation. Acta Mater. 55, 6843–6851.

Kollmann, H.T., Abueidda, D.W., Koric, S., Guleryuz, E., Sobh, N.A., 2020. Deep learning for topology optimization of 2D metamaterials. Mater. Des. 196, 109098.

Krose, B., Smagt, P.v.d., 2011. An introduction to neural networks.

Krogh, A., Hertz, J., 1992. A simple weight decay can improve generalization. Advances in Neural Information Processing Systems, pp. 950–957.

Leamy, H.J., Warlimont, H., 1970. The elastic behaviour of NiCo alloys. Phys. Status Solidi (b) 37, 523–534.

Li, W., Chen, S., Liaw, P.K., 2020. Discovery and design of fatigue-resistant high-entropy alloys. Scr. Mater. 187, 68–75.

Li, W., Lu, S., Hu, Q.-.M., Kwon, S.K., Johansson, B., Vitos, L., 2014. Generalized stacking fault energies of alloys. J. Phys. Condens. Matter 26, 265005.

Li, X., Schönecker, S., Vitos, L., Li, X., 2022. Generalized stacking faults energies of face-centered cubic high-entropy alloys: a first-principles study. Intermetallics 145, 107556.

Mohammed, A.S.K., Celebi, O.K., Sehitoglu, H., 2022. Critical stress prediction upon accurate dislocation core description. Acta Mater. 233, 117989.

Mohammed, A.S.K., Sehitoglu, H., 2020. Martensitic twin boundary migration as a source of irreversible slip in shape memory alloys. Acta Mater. 186, 50–67.

Müller, B., Reinhardt, J., Strickland, M.T., 1995. Neural Networks: an Introduction. Springer Science & Business Media.

Nabarro, F.R.N., 1947. Dislocations in a simple cubic lattice. Proc. Phys. Soc. 59 (2), 256–272.

Neighbours, J.R., Smith, C.S., 1954. The elastic constants of copper alloys. Acta Metall. 2, 591–596.

Nöhring, W.G., Curtin, W.A., 2020. Design using randomness: a new dimension for metallurgy. Scr. Mater. 187, 210–215.

Panchal, J.H., Kalidindi, S.R., McDowell, D.L., 2013. Key computational modeling issues in Integrated Computational Materials Engineering. Comput. Aided Des. 45, 4–25.

Peierls, R., 1940. The size of a dislocation. Proc. Phys. Soc. 52 (1), 34–37.

Ritchie, R.O., 2021. Toughening materials: enhancing resistance to fracture. Philos. Trans. R. Soc. A 379, 20200437.

Schoeck, G., 2005. The Peierls model: progress and limitations. Mater. Sci. Eng. A 400-401, 7–17.

Shahane, S., Guleryuz, E., Abueidda, D.W., Lee, A., Liu, J., Yu, X., Chiu, R., Koric, S., Aluru, N.R., Ferreira, P.M., 2022. Surrogate Neural Network model for sensitivity analysis and uncertainty quantification of the mechanical behavior in the optical lens-barrel assembly. Comput. Struct. 270, 106843.

Sidharth, R., Mohammed, A.S.K., Abuzaid, W., Sehitoglu, H., 2021. Unraveling frequency effects in shape memory alloys: NiTi and FeMnAlNi. Shape Mem. Superelasticity 7, 235–249.

Siegel, D.J., 2005. Generalized stacking fault energies, ductilities, and twinnabilities of Ni and selected Ni alloys. Appl. Phys. Lett. 87, 121901.

Simmons, G., Wang, H., 1971. Single crystal elastic constants and calculated aggregate properties, 2nd ed. MIT Press.

Söderlind, P., Eriksson, O., Wills, J.M., Boring, A.M., 1993. Theory of elastic constants of cubic transition metals and alloys. Phys. Rev. B 48, 5844–5851.

Stroh, A.N., 1958. Dislocations and cracks in anisotropic elasticity. Philos. Mag. 3, 625–646.

Tian, F., Varga, L.K., Chen, N., Delczeg, L., Vitos, L., 2013. Ab initio investigation of high-entropy alloys of 3d elements. Phys. Rev. B 87, 075144.

Werner, K.V., Niessen, F., Villa, M., Somers, M.A.J., 2021. Experimental validation of negative stacking fault energies in metastable face-centered cubic materials. Appl. Phys. Lett. 119, 141902.

Wills, J.M., Eriksson, O., Söderlind, P., Boring, A.M., 1992. Trends of the elastic constants of cubic transition metals. Phys. Rev. Lett. 68, 2802–2805.

You, D., Zhang, H., Ganorkar, S., Kim, T., Schroers, J., Vlassak, J.J., Lee, D., 2022. Electrical resistivity as a descriptor for classification of amorphous versus crystalline phases of alloys. Acta Mater. 231, 117861.